arXiv:2101.02821v3 [physics.flu-dyn] 25 Jul 2021

Dynamics of droplets under electrowetting effect with voltages exceeding the contact angle saturation threshold

Quoc Vo[1]†, and Tuan Tran[1]‡

[1]School of Mechanical & Aerospace Engineering, Nanyang Technological University, 50 Nanyang Avenue, 639798, Singapore

(Received xx; revised xx; accepted xx)

Electrowetting-on-dielectric (EWOD) is a powerful tool in many droplet-manipulation applications with a notorious weakness caused by contact-angle saturation (CAS), a phenomenon limiting the equilibrium contact angle of an EWOD-actuated droplet at high applied voltage. In this paper, we study the spreading behaviours of droplets on EWOD substrates with the range of applied voltage exceeding the saturation limit. We experimentally find that at the initial stage of spreading, the driving force at the contact line still follows the Young-Lippmann law even if the applied voltage is higher than the CAS voltage. We then theoretically establish the relation between the initial contact-line velocity and the applied voltage using the force balance at the contact line. We also find that the amplitude of capillary waves on the droplet surface generated by the contact line's initial motion increases with the applied voltage. We provide a working framework utilising EWOD with voltages beyond CAS by characterising the capillary waves formed on the droplet surface and their self-similar behaviours. We finally propose a theoretical model of the wave profiles taking into account the viscous effects and verify this model experimentally. Our results provide avenues to utilise the EWOD effect with voltages beyond CAS threshold and have strong bearing on emerging applications such as digital microfluidic and ink-jet printing.

Key words: Authors should not enter keywords on the manuscript, as these must be chosen by the author during the online submission process and will then be added during the typesetting process (see http://journals.cambridge.org/data/relatedlink/jfm-keywords.pdf for the full list)

1. Introduction

Contact angle of an electrically conductive droplet on an electrode covered by a dielectric layer reduces when a voltage U is applied between the droplet and the electrode (see Fig. 1a). This phenomenon, known as electrowetting-on-dielectric (EWOD), is one of the most effective techniques for droplet manipulation in three dimensional digital microfluidics (Jun Lee et al. 2012; Hong & Lee 2015), anti-icing (Mishchenko et al. 2010), self-cleaning (Blossey 2003) and control of droplet deposition (Baret & Brinkmann 2006). At low applied voltages, the equilibrium contact angle θ_e after U is applied directly relates

† Email address for correspondence: xqvo@ntu.edu.sg
‡ Email address for correspondence: ttran@ntu.edu.sg

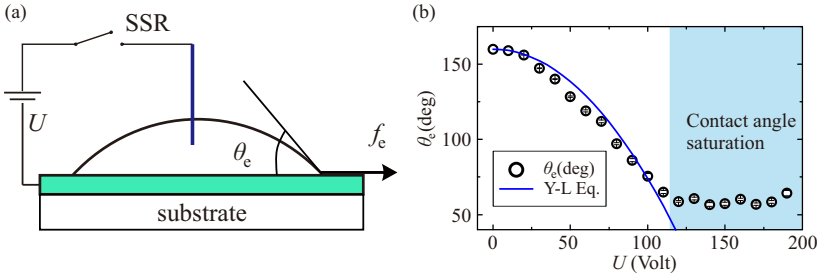


FIGURE 1. (a) Schematic showing the EWOD setup. (b) Plot showing the dependence of the equilibrium contact angle θ_e on the applied voltage U. The solid curve represents Eq. 1.1 without any fitting parameter. Contact angle saturation is observed for $U \geqslant U_s \approx 110\,\text{V}$.

to the voltage U and droplet's initial contact angle θ_0 via the so-called Young-Lippmann equation (Mugele & Baret 2005):

$$\cos\theta_e - \cos\theta_0 = \frac{\epsilon\epsilon_0 U^2}{2\sigma d}, \tag{1.1}$$

where ϵ_0 is the permittivity of free space; ϵ and d are, respectively, the dielectric constant and thickness of the dielectric coating, σ is surface tension of the droplet. When the applied voltage is sufficiently high, θ_e fails to follow Eq. 1.1 and is limited by a phenomenon known as contact angle saturation (CAS) (see Fig. 1b).

While transient behaviours of droplets under electrowetting actuation within the saturation limit are well-established (Mugele & Baret 2005; Vo & Tran 2018; Vo et al. 2018), the dynamics of droplets with applied voltage exceeding the CAS threshold remains elusive. Consequently, most applications utilising electrowetting uses applied voltage within the saturation value, U_s, a requirement significantly limiting EWOD's capabilities, especially in manipulating small and viscous droplets (Vo & Tran 2019; Fair 2007). Therefore, it is of practical importance to explore how droplet spreading dynamics is affected when the applied voltage is higher than the CAS threshold.

In this paper, we investigate the transient behaviours of droplets when the applied voltage U is higher than the CAS voltage U_s. We focus on small droplets with radius below capillary length and study their spreading behaviours in silicone oil medium under electrowetting actuation. We reveal a direct influence of increasing the applied voltage on enhancing the initial spreading velocity of droplets even when $U \geqslant U_s$. We also observe strong capillary waves on the droplet-oil interface and analyse their occurrence with the enhancement of the initial spreading velocity. We then propose and verify a theoretical model to explain the relation between the capillary waves under electrowetting actuation and the applied voltage.

2. Experimental setup, materials and method

In our experiment, we prepare test substrates using indium-tin-oxide (ITO) glass slides, each covered by a layer of fluoropolymer (Teflon, Dupont) having thickness $d = 2.5\mu\text{m}$. We dip an $18\,\mu$m-wire electrode made of tungsten into the droplet and connect it to the positive terminal of a DC power supply via a solid state relay (SSR) (see Fig. 1a), while the negative terminal to the ITO layer. The voltage applied to the two electrodes takes the form of a step function having amplitude U and duration T_p; the duration T_p is set sufficiently long to ensure that droplets under the electrowetting effect reach new equilibrium in every actuation. The amplitude U is varied between 0 V to 190 V. The

contact angle saturation voltage (CAS) is experimentally determined at $U_s = 110\,\mathrm{V}$ by observing the saturation behaviour of the contact angle when U is gradually increased (Fig. 1b). We note that the observed change of the equilibrium contact angle θ_e follows the Young-Lippmann equation (Eq. 1.1) when $U < U_s$ (Fig. 1b, solid curve).

We use a 0.125 M sodium chloride aqueous solution to generate droplets. For each experiment, we immerse a droplet and the substrate in silicone oil having viscosity $\mu_o = 1.8\,\mathrm{mPas}$. The interfacial tension of the solution in the silicone oil is measured experimentally at $\sigma = 37.2 \pm 0.5\,\mathrm{mPa\,s}$. The temperature of the oil pool is kept at $20 \pm 0.5\,^{\circ}\mathrm{C}$ to maintain consistent experimental conditions. The radius of the droplet is $R = 0.5\,\mathrm{mm}$, well below the capillary length $l_c = [\sigma/(\rho - \rho_o)g]^{1/2} = 5.5\,\mathrm{mm}$. Here, $g = 9.781\,\mathrm{m\,s^{-1}}$ is the gravitational acceleration, $\rho = 1000\,\mathrm{kg\,m^{-3}}$ and $\rho_o = 873\,\mathrm{kg\,m^{-3}}$ the density of the working liquid and the oil, respectively. We capture the behaviours of droplets using a high speed camera (Photron, SAX2) typically running at 5000 frame-per-second.

3. Results and Discussions

3.1. *Spreading dynamics by electrowetting beyond contact angle saturation*

In Fig. 2a, we show several series of snapshots of droplets shortly after a voltage U is applied. Generally, we observe that higher applied voltage causes more violent spreading behaviours due to larger contact-line tension imbalance (Mugele & Baret 2005). For instance, at $U = 60\,\mathrm{V}$ (Fig. 2a, first panel), the droplet gently spreads and maintains its spherical shape at all time. At $U = 90\,\mathrm{V}$ (Fig. 2a, second panel), faster contact-line motion generates capillary waves on the liquid-oil interface and consequently causes substantial deformation to the droplet's shape. When the voltage increases above 120 V, the capillary waves become so strong that the deformation at the liquid-oil interface causes small satellite droplets to eject from the primary droplets (Fig. 2a, two last panels). In such droplet-ejection instances, the size of the satellite droplets increases when U varies from 120 V to 150 V.

Surprisingly, we also observe from Fig. 2a that droplet deformation increases with the applied voltage even at $U \geqslant U_s = 110\,\mathrm{V}$. As the deformation is caused by the capillary waves originated from the contact-line initial motion, we hypothesise that CAS causes little effect to the early dynamics of the contact line. In Fig. 2b, we show how the contact-line velocity v_{ct} depends on time for several values of U from 30 V to 170 V. We observe that when $U < U_s$, increasing U shifts the velocity curves upwards, indicating that both early-time and late-time spreading dynamics are affected by the applied voltage (Fig. 2b, open markers). However, when $U > U_s$, escalating U only increases the initial values of v_{ct}. Subsequently, v_{ct} of all the values of $U > U_s$ converse to the same curve (Fig. 2b, solid markers). This observation confirms that the contact-line initial velocity and the resulting capillary waves on the droplet's surface are not limited by CAS; CAS only affects the late-time spreading dynamics of the droplets.

In Fig. 2c, we show the initial contact-line velocity v_i, i.e., v_{ct} measured at $t = 0$, vs. the applied voltage U. We observe that although v_i increases with U in the whole range of the applied voltage, the increasing rate of v_i is higher for $U < 90\,\mathrm{V}$ compared to that for $U \geqslant 90\,\mathrm{V}$. Beyond the critical voltage $U_c = 90\,\mathrm{V}$, determined where the switch in the increasing rate of v_i occurs, it is possible to observe capillary waves on the droplet-oil interface (see Fig. 2a). The occurrence of the capillary waves when the applied voltage is increased beyond U_c suggests that the initial driving force generated by the electrowetting effect is opposed by the resistive force at the contact line for $U < U_c$,

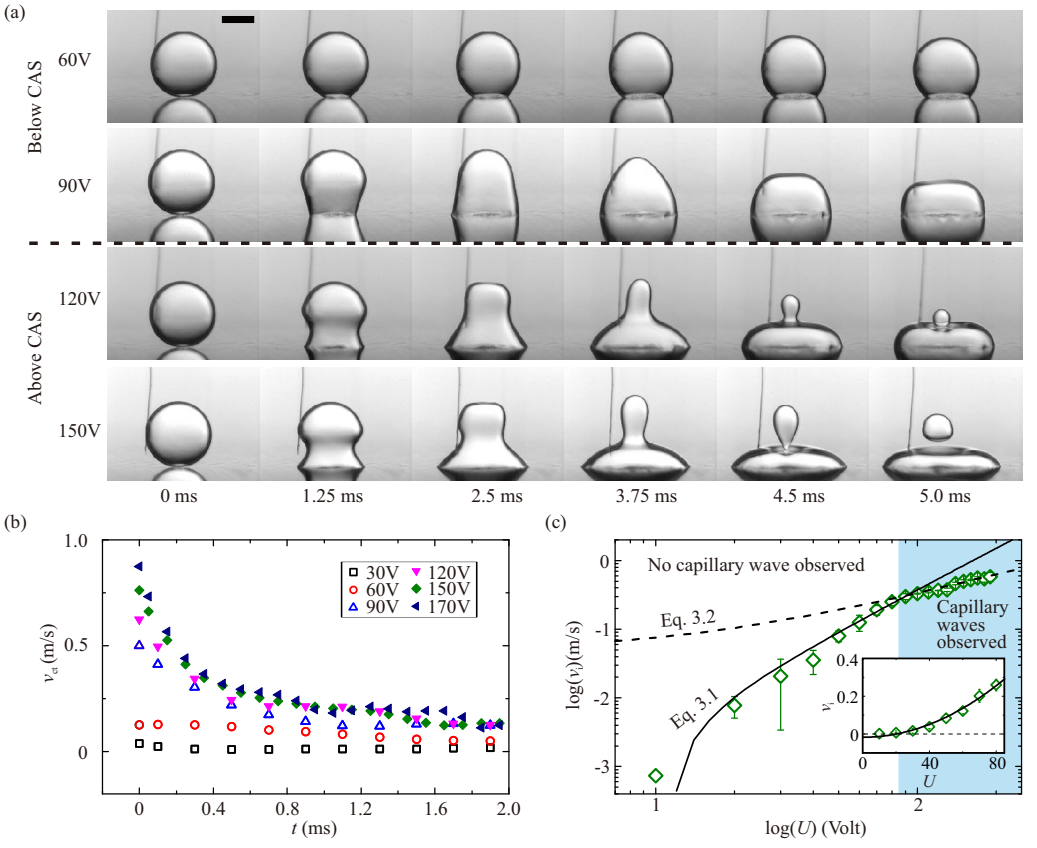


FIGURE 2. (a) Snapshots showing the contact-line behaviours of droplets under different applied voltages U varying from 60 V to 150 V. The scale bar represents 0.5 mm. Capillary waves on droplet's surface are observed when $U \geqslant 90$ V. (b) Plot showing the contact-line velocity v_{ct} vs. time t: open markers for those of voltage below the saturation value, i.e., $U < 110$ V; solid markers for those of voltage above the saturation value, i.e., $U > 110$ V. (c) Log-log plot showing the initial contact-line velocity v_i vs. the applied voltage U. Inset: Linear plot of v_i vs. U for $U < 90$ V, the voltage's range in which no capillary wave is observed on the droplet's surface.

and by the droplet's inertia for $U \geqslant U_c$. As a result, the relation between v_i and U can be obtained by balancing the driving force $f_e = \epsilon\epsilon_0(2d)^{-1}U^2$, resulted from strong localisation of the electrical field at the contact line (Mugele & Baret 2005), and either the resitive force $v_i\lambda + f$ for $U < U_c$, or inertia $\rho r_0 v_i^2$ for $U \geqslant U_c$. Here, λ is the contact-line friction coefficient described by the geometric mean of the droplet's viscosity and the oil's viscosity (Vo & Tran 2018), and f is the contact-line elasticity force caused by microscopic defects on the surface (De Gennes 1985; Joanny & de Gennes 1984). If we assume that $f_e = \epsilon\epsilon_0(2d)^{-1}U^2$ is independent from CAS in the early-time dynamic, we obtain

$$v_i = \epsilon\epsilon_0(2d\lambda)^{-1}U^2 - f\lambda^{-1} \qquad \text{for } U \leqslant U_c = 90\,\text{V}, \tag{3.1}$$

$$v_i = (\epsilon\epsilon_0)^{1/2}(2d\rho r_0)^{-1/2}(U - U_c) + v_c \qquad \text{for } U \geqslant U_c = 90\,\text{V}, \tag{3.2}$$

where $v_c = \epsilon\epsilon_0(2d\lambda)^{-1}U_c^2 - f\lambda^{-1}$ is the critical contact-line velocity above which the capillary wave is observed on the droplet-oil interface. In our experiment, $v_c = 0.3\,\text{ms}^{-1}$. In Fig. 2c, we plot both Eq. 3.1 (solid lines in the main figure and the inset) and Eq. 3.2 (dashed line). We observe an excellent agreement between the experimental data and

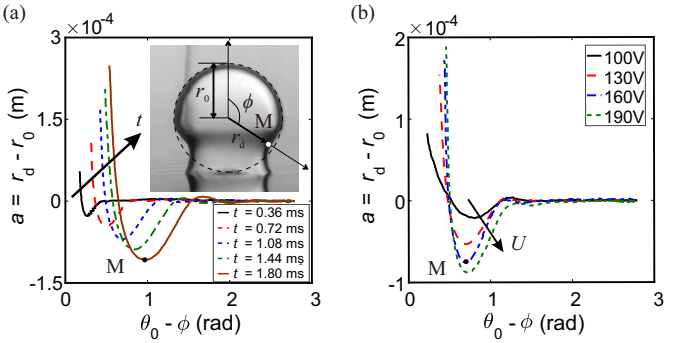


FIGURE 3. (a) Plot showing the displacement a vs. the wave's position $\theta_0 - \phi$ of the capillary waves propagating along the droplet-oil interface at different time t when $U = 150\,\mathrm{V}$ is applied. (b) Plot showing a vs. $\theta_0 - \phi$ of the capillary waves at $t/\tau = 1$ and at different applied voltages varying from 100 V to 190 V. Here, $\tau = (\rho r_0^3/\sigma)^{1/2}$ is the inertia-capillary time. The maximum displacement (at point M) increases with the applied voltage regardless of CAS.

both equations in their respective validity ranges. Best fit of Eq. 3.1 to the data in Fig. 2c gives $\lambda = 0.075 \pm 0.005\,\mathrm{Pa\,s}$, in good agreement with the previously reported values for contact-line friction coefficient in the same systems ($\lambda \approx 0.1 \pm 0.01\,\mathrm{Pa\,s}$) (Vo et al. 2018; Vo & Tran 2018). The fitting also reveals the contact-line elasticity force $f = (2.1 \pm 0.2) \times 10^{-3}\,\mathrm{Nm^{-1}}$, which is of the same order of the previously reported value, i.e., $(8.6 \pm 0.9) \times 10^{-3}\,\mathrm{Nm^{-1}}$ in Vo & Tran (2019).

3.2. *Capillary waves*

Fast contact line motion generated by the electrowetting effect when $U \geqslant U_c$ causes capillary waves on the droplet's surface. A remarkable feature of the generated capillary waves is that their amplitude increase with the applied voltage U even when U is higher than the CAS voltage (see Fig. 2). To exploit this feature in practical applications, e.g., manipulating small and viscous droplets (Vo & Tran 2019; Fair 2007), inducing droplet jumping by modulating actuation time (Wang et al. 2017), and controlling droplet ejection (Vo & Tran 2021), we examine the induced capillary waves on the water-oil interface to reveal the dependence of the wave amplitude on the applied voltage.

3.2.1. *Capillary-wave generation*

To induce capillary waves on the surface of a droplet, the contact-line velocity has to overcome the inertial-capillary velocity $(\sigma/\rho r_0)^{1/2}$, formulated using the stabilising velocity of a deformed droplet's surface to minimise its curvature (Taylor 1959). In normal wetting phenomena, the maximum velocity of the contact line that can be theoretically achieved is σ/λ. As a result, the condition enabling capillary waves becomes $\sigma/\lambda \geqslant (\sigma/\rho r_0)^{1/2}$, or $\xi = \lambda/(\sigma\rho r_0)^{1/2} \leqslant 1$. Here, the so-called damping coefficient ξ measures the viscous effects in both the droplet and the outer oil against inertia for capillary flows. We note that ξ is defined similarly to the Ohnesorge number $\mathrm{Oh} = \mu/(\sigma\rho r_0)^{1/2}$, where μ is the liquid viscosity. In wetting phenomena driven by the electrowetting effect, v_i is determined by Eq. 3.1 and Eq. 3.2, resulting in another condition for capillary waves to occur: $v_i \geqslant (\sigma/\rho r_0)^{1/2}$. Using the experimental parameters in our experiment, the condition for the contact-line velocity to generate capillary waves is $v_i \geqslant (\sigma/\rho r_0)^{1/2} = 0.27\,\mathrm{ms^{-1}}$, consistent with our experimental results shown in Fig. 2c, i.e., capillary waves are observable when $v_i \geqslant 0.3\,\mathrm{ms^{-1}}$. We note that if we define a Weber-like number $\mathrm{We} = v_i^2 \rho r_0/\sigma$, the condition for capillary waves to occur then takes the form $\mathrm{We} \geqslant 1$.

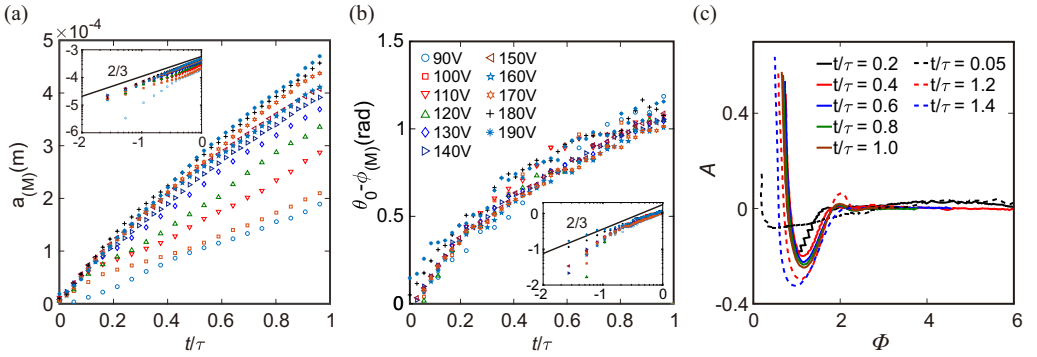


FIGURE 4. (a) Plot showing the displacement of point M, $a_{(\mathrm{M})}$, vs. t/τ for U varying from 90 V to 190 V. Inset: Log-log plot of the data in the main plot showing the power law dependence $a_{(\mathrm{M})} \sim (t/\tau)^{2/3}$. The legends are given in (b). (b) Plot showing the wave's position of point M, $\theta_0 - \phi_{(\mathrm{M})}$, vs. t/τ for U varying from 90 V to 190 V. Inset: Log-log plot of the data in the main plot revealing the power law dependence $\phi_0 - \phi_{(\mathrm{M})} \sim (t/\tau)^{2/3}$. (c) Plot showing the dimensionless displacement A vs. the dimensionless wave's position Φ at different values of t/τ varying from 0.05 to 1.4. We observe self-similar behaviours of the capillary waves for $0.2 \leqslant t/\tau \leqslant 1$ (solid curves). Whereas the capillary waves are not self-similar for $t/\tau < 0.2$ and $t/\tau > 1$ (dashed curves).

3.2.2. *Capillary-wave characteristics*

To quantify the amplitude and phase of the capillary waves on a droplet having spherical-cap radius r_s and contact angle θ_0, we use a polar coordinate system (r, ϕ) with origin $(r = 0, \phi = 0)$ at a distance r_s below the droplet's apex and the polar axis vertically upward (Fig. 3a, inset). For droplets in our experiment, $\theta_0 \approx \pi$ and $r_\mathrm{s} \approx r_0$. In this coordinate system, the droplet-oil profile, which is also the capillary waveform, is $(r_\mathrm{d}, \theta_0 - \phi)$, where θ_0 is the wave's position of the contact line at $t = 0$. The displacement of the capillary wave is therefore $a = r_\mathrm{d} - r_s$, measured by the deviation of the droplet-oil interface from the droplet's initial shape $(r_d = r_s)$. In Fig. 3a, we show a vs. $\theta_0 - \phi$ at several instances of time t when $U = 150\,\mathrm{V}$ is applied. When t increases, the waveform moves from left to right indicating that the wave propagates further from the contact line and towards the apex of the droplet $(\phi = 0)$. Furthermore, we observe that while the wave's propagating velocity reduces with time, its amplitude increases suggesting that the wave's kinetic energy, originated from the fast initial motion of the contact line, is progressively converted to surface energy during its propagation.

In Fig. 3b, we show a plot of a vs. $\theta_0 - \phi$ at $t = \tau$ for different values of U varying from 100 V to 190 V. Here, $\tau = (\rho r_0^3/\sigma)^{1/2}$ is the inertial-capillary time. We observe that the displacement at point M significantly increases with U, while the wave's position of the point M does not depend on U. This observation is examined more quantitatively in Fig. 4a and b where we respectively show $a_{(\mathrm{M})}$ and $\theta_0 - \phi_{(\mathrm{M})}$ vs. t/τ for all the values of U ranging from 90 V to 190 V. Here, $a_{(\mathrm{M})}$ and $\theta_0 - \phi_{(\mathrm{M})}$ denote the displacement and the position of the waves at point M, respectively. On the one hand, we observe that the slopes of $a_{(\mathrm{M})}$ vs. t/τ increase with U showing that the dependence of $a_{(\mathrm{M})}$ on t/τ is more strongly at higher applied voltages. On the other hand, $\theta_0 - \phi_{(\mathrm{M})}$ is independent from U at any values of t/τ indicating that the propagating velocity only depends on the hydrodynamical properties of the droplets, not the contact-line velocity.

The scaling laws for the displacement and the position of capillary waves on the surface of a spreading droplet were proposed by Ding et al. (2012) by adapting Keller & Miksis

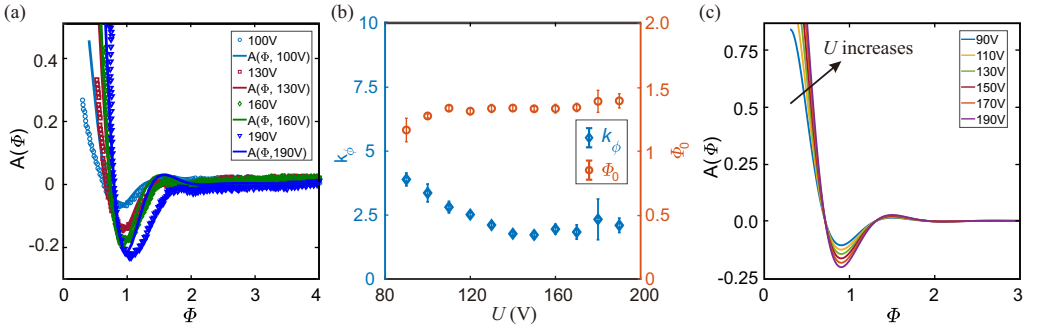


FIGURE 5. (a) Examples of fitting the experimental data of A vs. Φ at $t/\tau = 0.25$ to Eq. 3.10. Similar results are obtained for other values of t/τ varying from 0.2 to 1. (b) Plot showing the fitting parameters k_ϕ (on the left axis) and Φ_0 (on the right axis) vs. the applied voltage U. Both $k_\phi = 2.4 \pm 0.7$ and $\Phi_0 = 1.32 \pm 0.06$ appear to be constants in the voltage's range. (c) Plot representing Eq. 3.10 for different applied voltage varying from 90 V to 190 V, and with $k_\phi = 2.4$ and $\Phi_0 = 1.32$.

(1983)'s self-similarity theory for surface-tension driven flows:

$$a = Ar_0 \left(\frac{t}{\tau}\right)^{2/3} \text{ and } \theta_0 - \phi = \Phi \left(\frac{t}{\tau}\right)^{2/3}, \tag{3.3}$$

where A and Φ denote the dimensionless displacement and the dimensionless position of the waves, respectively. In the insets of Fig. 4a and b, we show the log-log plots of $a_{(\mathrm{M})}$ vs. t/τ and $\theta_0 - \phi_{(\mathrm{M})}$ vs. t/τ, respectively. We observe that $a_{(\mathrm{M})} \sim (t/\tau)^{2/3}$ and $\theta_0 - \phi_{(\mathrm{M})} \sim (t/\tau)^{2/3}$, implying that Eq. 3.3 is also applicable in our system in which the capillary waves are generated by electrowetting actuation. To further test Eq. 3.3, in Fig. 4c, we show the dimensionless waveforms, i.e., $A = ar_0^{-1}(t/\tau)^{-2/3}$ vs. $\Phi = (\theta_0 - \phi)(t/\tau)^{-2/3}$ when t/τ varies from 0.05 to 1.4. We observe that all the waveforms for $0.2 \leqslant t/\tau \leqslant 1$ collapse onto a single one confirming the self-similar behaviour of the capillary waves in this time range. However, we notice that capillary waves are not self-similar for $t/\tau < 0.2$ and $t/\tau > 1$ (see the dashed curves in Fig. 4c). At $t/\tau < 0.2$, i.e., a short time after wetting is initiated, the waves are local at the contact line region (Cox 1986), whereas, at $t/\tau > 1$ the capillary waves reach the apex of the droplet and start interacting with the waves coming from the other side of the droplet. As a result, at both extremes the capillary waves on the droplet's surface are more complicated and cannot be described by a single self-similar scaling law.

3.2.3. *Profiles of capillary waves*

With the self-similar behaviour of the capillary waves, it is possible to reduce the wave's profile $a(\phi, t)$ at any time t by a time-invariant dimensionless profile $A(\Phi)$. The first solution for $A(\Phi)$ was proposed by Keller & Miksis (1983) who modified the calculation of Jeffreys & Jeffreys (1999) for inviscid, self-similar capillary-driven flows in a fluid wedge. Later, Billingham (1999) theoretically incorporated viscosity effects using the capillary-viscosity velocity. However, both Keller & Miksis (1983)'s and Billingham (1999)'s solutions fail to fit our experimental data. While Keller & Miksis (1983)'s lacks of the viscous effects, the model of Billingham (1999) is only applicable at a very early time after the wave is generated, and in a very small region close to the wave's source, e.g., the time and length scales respectively are ≈ 0.2 ns and ≈ 10 nm for water.

We seek an alternative expression of $A(\Phi)$ taking into account the viscosity effect in our system. The self-similar profiles $A(\Phi)$ (see the profiles of $0.2 \leqslant t/\tau \leqslant 1$ in Fig. 4c) can

be approximated by spatially decaying waves driven by interfacial tension and resisted by inertia and viscous forces. For such waves, we expect that $A(\Phi)$ is the solution of an one-dimensional time-invariant wave equation with a spatial damping coefficient $\xi = \lambda/(\sigma\rho r_0)^{1/2}$:

$$\frac{d^2A}{d\Phi^2} + 2k\xi\frac{dA}{d\Phi} + k^2A = 0, \tag{3.4}$$

where $k = 2\pi/\lambda_\Phi = 2\pi$ is the wave number, $\lambda_\Phi = 1$ is the dimensionless wavelength. We note that the damping coefficient ξ does not depend on the strength of the driving force at the contact line. Our discussion is also limited to the case that $\xi < 1$ for the possibility of capillary wave generation as discussed in Section. 3.2.1.

If we denote $\Phi_0 \geqslant 0$ the dimensionless position of the contact line, the profile A in Eq. 3.4 is required to satisfy the following boundary conditions:

$$A\Big|_{\Phi=\Phi_0} = A_{\rm ct} = \frac{a_{\rm ct}}{r_0(t/\tau)^{2/3}}, \tag{3.5}$$

$$\frac{dA}{d\Phi}\Big|_{\Phi=\Phi_0} = \frac{dA_{\rm ct}}{d\Phi_{\rm ct}} = \frac{\dot{a}_{\rm ct}r_0^{-1} - (2/3)a_{\rm ct}r_0^{-1}t^{-1}}{-\dot{\phi}_{\rm ct} - (2/3)(\theta_0 - \phi_{\rm ct})t^{-1}}, \tag{3.6}$$

where $a_{\rm ct} = r_{\rm ct}(\sin\phi_{\rm ct})^{-1} - r_0$ is the contact line's displacement, $\phi_{\rm ct}$ its wave's position, $r_{\rm ct}$ the contact radius, $\dot{a}_{\rm ct}$ denotes the time derivatives of $a_{\rm ct}$ and $\phi_{\rm ct}$ the time derivatives of $\dot{\phi}_{\rm ct}$. As we consider the capillary waves generated short-time after the electrowetting effect is activated, we can approximate $a_{\rm ct} \approx 0$, $\phi_{\rm ct} \approx \theta_0$, $a_{\rm ct}t^{-1} \approx \dot{a}_{\rm ct} \approx v_{\rm i}\sin\theta_0$ and $-(\theta_0 - \phi_{\rm ct})t^{-1} \approx \dot{\phi}_{\rm ct} = -k_\phi r_0^{-1}(\sigma/\rho r_0)^{1/2}$, where k_ϕ is a positive constant. As a result, we obtain

$$A\Big|_{\Phi=\Phi_0} = 0, \tag{3.7}$$

$$\frac{dA}{d\Phi}\Big|_{\Phi=\Phi_0} = \frac{v_{\rm i}\sin\theta_0}{k_\phi(\sigma/\rho r_0)^{1/2}} = \frac{{\rm We}^{1/2}\sin\theta_0}{k_\phi}. \tag{3.8}$$

The general solution of Eq. 3.4 is

$$A = {\rm e}^{-k\xi(\Phi-\Phi_0)}\left[\alpha\cos k_{\rm d}(\Phi - \Phi_0) + \beta\sin k_{\rm d}(\Phi - \Phi_0)\right]. \tag{3.9}$$

Here, $k_{\rm d} = 2\pi(1-\xi^2)^{1/2}$ is the attenuated wave number due to the damping coefficient ξ. Applying Eq. 3.7 and Eq. 3.8 to Eq. 3.9, we obtain $\alpha = 0$ and $\beta = {\rm We}^{1/2}\sin\theta_0(k_{\rm d}k_\phi)^{-1}$. Consequently, we obtain an explicit expression of $A(\Phi)$:

$$A = \frac{{\rm We}^{1/2}\sin\theta_0}{k_\phi k_{\rm d}}\,{\rm e}^{-k\xi(\Phi-\Phi_0)}\,\sin[k_{\rm d}(\Phi - \Phi_0)]. \tag{3.10}$$

To verify Eq. 3.10, we use the least-mean-square method to fit the experimental data of A vs. Φ to Eq. 3.10 with the fitting parameters Φ_0 and k_ϕ. Examples of the fittings at $t/\tau = 0.25$ and for different applied voltages U are shown in Fig. 5a. Similar results obtained for different values of t/τ varying from 0.2 to 1 indicate a good agreement between Eq. 3.10 and the experimental data. In Fig. 5b, we show the values of k_ϕ (left axis) and Φ_0 (right axis) that both can be approximated as constants, i.e., $k_\phi = 2.4 \pm 0.7$ and $\Phi_0 = 1.32 \pm 0.06$, for U varying from 90 V to 190 V. All solutions for $90 \leqslant U \leqslant 190$ V are plotted in Fig. 5c.

4. Conclusions

We have shown that the initial contact-line velocity of a droplet spreading on a solid substrate under the electrowetting effect is not affected by the contact angle saturation (CAS). We theoretically derived and experimentally verified the relation between the initial contact-line velocity and the applied voltage. The magnitude of the capillary waves on the droplet-oil interface also depends on the applied voltage regardless of CAS. Based on theories describing the self-similar behaviours of interfacial-tension-driven flows, we then proposed a mathematical expression and provided experimental verification for the far-field capillary-wave profiles incorporating viscous effects. The proposed model strengthens our current understanding on how the capillary waves generates, propagates and decays. The model is also useful in understanding other capillary-wave-driven phenomena such as droplet jumping (Vahabi et al. 2018), droplet/bubble ejection by coalescence (Zhang et al. 2015; Zhang & Thoroddsen 2008; Zhang et al. 2009), bubble-busting jet at liquid-air interface (Gordillo & Rodríguez-Rodríguez 2019), and bouncing of impacting droplets on a solid substrate (Richard et al. 2002; Renardy et al. 2003).

Acknowledgments

This study is supported by Nanyang Technological University, the Republic of Singapore's Ministry of Education (MOE, Grant No. MOE2018-T2-2-113), and the Agency for Science, Technology and Research (A*STAR, Grant No. 1523700102).

Declaration of Interests

The authors report no conflict of interest.

REFERENCES

Baret, J.-C. & Brinkmann, M. 2006 Wettability Control of Droplet Deposition and Detachment. *Phys. Rev. Lett.* **96**, 146106.

Billingham, J. 1999 Surface-tension-driven flow in fat fluid wedges and cones. *J. Fluid Mech.* **397**, 45–71.

Blossey, R. 2003 Self-cleaning surfaces — virtual realities. *Nat. Mater.* **2**, 301–306.

Cox, R. G. 1986 The dynamics of the spreading of liquids on a solid-surface. Part 1. Viscous-flow. *J. Fluid Mech.* **168**, 169–194.

De Gennes, P. G. 1985 Wetting: Statics and dynamics. *Rev. Mod. Phys.* **57**, 827–863.

Ding, H., Li, E. Q., Zhang, F. H., Sui, Y., Spelt, P. D. M. & Thoroddsen, S. T. 2012 Propagation of capillary waves and ejection of small droplets in rapid droplet spreading. *J. Fluid Mech.* **697**, 92–114.

Fair, R. B. 2007 Digital microfluidics: is a true lab-on-a-chip possible? *Microfluid. Nanofluidics* **3**, 245–281.

Taylor, G. I. 1959 The dynamics of thin sheets of fluid. III. Disintegration of fluid sheets. *Proc. R. Soc. London. Ser. A. Math. Phys. Sci.* **253** (1274), 313–321.

Gordillo, J. M. & Rodríguez-Rodríguez, J. 2019 Capillary waves control the ejection of bubble bursting jets. *J. Fluid Mech.* **867**, 556–571.

Hong, J. & Lee, S. J. 2015 Detaching droplets in immiscible fluids from a solid substrate with the help of electrowetting. *Lab Chip* **15** (3), 900–907.

Jeffreys, H. & Jeffreys, B. 1999 *Methods of Mathematical Physics, 3rd edition.* Cambridge University Press.

Joanny, J. F. & de Gennes, P. G. 1984 A model for contact angle hysteresis. *J. Chem. Phys.* **81** (1), 552–562.

Jun Lee, S., Lee, S. & Kang, K. H. 2012 Droplet jumping by electrowetting and its application to the three-dimensional digital microfluidics. *Appl. Phys. Lett.* **100** (8), 081604.

Keller, J. B. & Miksis, M. J. 1983 Surface Tension Driven Flows. *SIAM J. Appl. Math.* **43** (2), 268–277.

Mishchenko, L., Hatton, B., Bahadur, V., Taylor, J. A., Krupenkin, T. & Aizenberg, J. 2010 Design of Ice-free Nanostructured Surfaces Based on Repulsion of Impacting Water Droplets. *ACS Nano* **4** (12), 7699–7707.

Mugele, F. & Baret, J.-C. 2005 Electrowetting: from basics to applications. *J. Phys. Condens. Matter* **17** (28), R705–R774.

Renardy, Y., Popinet, S., Duchemin, L., Renardy, M., Zaleski, S., Josserand, C., Drumright-Clarke, M. A., Richard, D., Clanet, C. & Quéré, D. 2003 Pyramidal and toroidal water drops after impact on a solid surface. *J. Fluid Mech.* **484** (484), 69–83.

Richard, D., Clanet, C. & Quéré, D. 2002 Contact time of a bouncing drop. *Nature* **417** (6891), 811.

Vahabi, H., Wang, W., Mabry, J. M. & Kota, A. K. 2018 Coalescence-induced jumping of droplets on superomniphobic surfaces with macrotexture. *Sci. Adv.* **4** (11), 1–8.

Vo, Q., Su, H. & Tran, T. 2018 Universal Transient Dynamics of Electrowetting Droplets. *Sci. Rep.* **8** (1), 836.

Vo, Q. & Tran, T. 2018 Contact line friction of electrowetting actuated viscous droplets. *Phys. Rev. E* **97** (6), 063101.

Vo, Q. & Tran, T. 2019 Critical conditions for jumping droplets. *Phys. Rev. Lett.* **123** (2), 024502.

Vo, Q. & Tran, T. 2021 Droplet ejection by electrowetting actuation. *Appl. Phys. Lett.* **118** (2), 161603.

Zhang, F. H., Li, E. Q. & Thoroddsen, S. T. 2009 Satellite formation during coalescence of unequal size drops. *Phys. Rev. Lett.* **102** (10), 104502.

Zhang, F. H., Thoraval, M. J., Thoroddsen, S. T. & Taborek, P. 2015 Partial coalescence from bubbles to drops. *J. Fluid Mech.* **782**, 209–239.

Zhang, F. H. & Thoroddsen, S. T. 2008 Satellite generation during bubble coalescence. *Phys. Fluids* **20** (2), 022104.

Wang, Z., Ende, D. van den, Pit, A., Lagraauw, R., Wijnperle, D. & Mugele, F. 2017 Jumping drops on hydrophobic surfaces, controlling energy transfer by timed electric actuation. *Soft Matter* **13**, 4856-4863.